J Mater Sci (2008) 43:244–253
DOI 10.1007/s10853-007-2173-x

The modification of MoO_3 nanoparticles supported on mesoporous SBA-15: characterization using X-ray scattering, N_2 physisorption, transmission electron microscopy, high-angle annular darkfield technique, Raman and XAFS spectroscopy

Zhida Huang · Wolfgang Bensch · Wilfried Sigle · Peter A. van Aken · Lorenz Kienle · Tonya Vitoya · Hartwig Modrow · Thorsten Ressler

Received: 15 March 2007 / Accepted: 17 September 2007 / Published online: 17 October 2007

Abstract MoO_3 was dispersed onto mesoporous SBA-15 by using ammonium heptamolybdate as MoO_3 source. The formation of MoO_3 was carried out by heating the loaded material to 500 °C for 3 h in air. Below 13 wt% Mo loading, no reflections of MoO_3 occur in the X-ray powder patterns and even for high MoO_3 contents, the intensities of the reflections are much lower than expected for fully crystalline material. A detailed XAFS analysis reveals that at low Mo contents, the metastable hexagonal modification of MoO_3 is formed despite the high calcination temperature of 500 °C. It is highly likely that the nanosize of the particles and the interaction between MoO_3 and SBA-15 stabilize the metastable modification of the material. Nitrogen physisorption experiments show the typical type-IV isotherms indicating that the mesoporosity of the materials is preserved despite the large amount of MoO_3. Transmission electron micrographs demonstrate the presence of MoO_3 inside the SBA-15 support. The Raman spectra display a remarkable size-dependent intensity loss and several features give evidences for a bond formation between nano-sized MoO_3 particles and the silica support. Moreover, the spectroscopic details suggest the formation of $(MoO_3)_n$ oligomers.

Z. Huang · W. Bensch (✉)
Institut für Anorganische Chemie, University of Kiel, Olshausenstraße 40-60, Kiel 24098, Germany
e-mail: wbensch@ac.uni-kiel.de

W. Sigle · P. A. van Aken
Max-Planck-Institut für Metallforschung, Heisenbergstr. 3, 70506 Stuttgart, Germany

L. Kienle
Max-Planck-Institut für Festkörperforschung, Heisenbergstr. 1, 70506 Stuttgart, Germany

T. Vitoya · H. Modrow
Physikalisches Institut der Universität Bonn, Nussallee 12, 53115 Bonn, Germany

T. Ressler
Institut für Chemie, Fachgruppe Anorganische und Analytische Chemie, TU Berlin, Straße des 17. Juni 135, 10623 Berlin, Germany

Introduction

In the past few years, periodic silica-based mesoporous materials such as MCM-41 and SBA-15 were used as templates for the syntheses of shape-selective new materials. The mesoporous materials are synthesized via the polymerization of silica around periodic cationic amphiphiles (MCM-41) and neutral block copolymer (SBA-15). SBA-15 possesses well-ordered hexagonal arrays of mesopores with pore diameters between 3 and 30 nm [1, 2] and SBA-15 possesses thicker walls (31–64 Å) compared to MCM-41. Therefore, SBA-15 exhibits a higher thermal stability, being claimed to be stable for at least 48 h in boiling water [1]. Using SBA-15 with the narrow pore diameter distribution as a template for the synthesis of nanoparticles, products are obtained reflecting the diameters of the pores and maximal particle lengths in accordance with the channel lengths of the template material. Such incorporated nanoparticles may have interesting optical, magnetic, and catalytic properties. In addition to the studies of the formation of metal nanoparticles and nanowires, such as Pt [3–5], Pd [6–9], Au [3–5, 10, 11], Ag [3], and Ti [12], the formation of binary nanomaterials such as PbS [13], CdS [14], TiN [15], and GaN [16] within the nanoscale channels of these

mesoporous materials have been explored. More recently, highly ordered quantum wires of $Zn_{1-x}Mn_xS$ [17] and $Cd_{1-x}Mn_xS$ [18] have been successfully synthesized within the mesopores of SBA-15.

Molybdenum-based catalysts have been investigated intensively [19–24] because of their importance in the technical processes, such as propene metathesis [25, 26], propene oxidation [27, 28], methanol oxidation [29], ethanol oxidative photochemical reaction, and most importantly in hydrodesulfurization (HDS) processes, which represent one of the largest groups of catalytic steps in petroleum and petrochemical reactions. Recently, SBA-15-supported MoO_3 materials were used as an intermediate for the preparation of MoS_2 catalysts. Different synthesis strategies were applied like thermal treatment of SBA-15 impregnated with ammonium heptamolybdate (AHM) [30], thermal spreading of MoO_3 [31], or sonochemical decomposition of $Mo(CO)_6$ in organic solvents [32]. The main aim of these investigations was the preparation of active HDS catalysts. The formation of MoO_3 and especially the structures of the supported oxide were not investigated. The MoO_3 species are formed within a confined space and the highly interesting question arises whether a metastable modification of the oxide is formed depending on particle sizes as observed for other oxides like TiO_2. The thermal decomposition of bulk AHM in different gas atmospheres was recently investigated by in-situ X-ray absorption spectroscopy (XAFS) and in-situ X-ray diffraction [33]. Under static condition AHM is decomposed first to an amorphous phase followed by the formation of ammonium tetramolybdate (ATM) at about 230 °C. With increasing temperature, first a mixture of α- and hexagonal MoO_3 is formed and finally pure orthorhombic α-MoO_3 is observed at about 360 °C. In the present study, AHM was decomposed to prepare MoO_3 species within the pores of SBA-15. Several samples containing different amounts of MoO_3 are analyzed and characterized applying various analytical methods including Raman spectroscopy, N_2 physisorption, transmission electron microscopy (TEM), high-angle annular darkfield (HAADF) technique combined with energy-dispersive X-ray analysis (EDXS), X-ray scattering experiments, and XAFS. From the results of these studies, a complete picture of the structures of MoO_3/SBA-15 composite materials is obtained.

Experimental section

Sample preparation

Synthesis of pristine mesoporous SBA-15

About 8 g of poly(ethylene glycol)-block-poly(propylene glycol)-block-poly(ethylene glycol) triblock copolymer (Aldrich, pluronic, P-123) was dissolved in 240 g of water and 28.6 g of concentrated HCl at 30 °C on a water bath. After dropwise addition of 16 g of tetraethyl orthosilicate (TEOS), the reaction mixture was stirred for 24 h at 30 °C. The resulting gel was transferred into a Teflon bottle and heated to 80 °C for 24 h to obtain SBA-15 with 6 nm pores. The resulting white powder was filtered and washed with deionized water, and the surfactant was removed by Soxleth extraction at 78 °C with a mixture of 970 mL of ethanol and 30 mL of concentrated hydrochloric acid. After washing with ethanol, the white powder was dried at RT for about 1 week.

Synthesis of MoO_3/SBA-15

Typically, 1 g of SBA-15 was stirred in aqueous solutions of ammonium heptamolybdate $(NH_4)_6Mo_7O_{24}$ $4H_2O$ (AHM) with different concentrations at pH 7–8. After stirring at room temperature for 18 h, the products were filtered without washing. The impregnated SBA-15 was calcined at 500 °C for 3 h in air to obtain MoO_3. This calcination temperature is much higher than the usual thermal decomposition temperature of AHM (ca. 350 °C) [34], at which MoO_3 is formed in air. At lower temperatures, AHM is found not completely to be decomposed to MoO_3, which indicates that AHM is located in the pores and not on the outer surface of the material. The silica walls and small pore diameters can impede the removal of the decomposition products of AHM, such as NH_3 and H_2O, and consequently a higher formation temperature is required. Materials containing different Mo concentrations were prepared using appropriate concentrations of AHM, i.e., 0.03, 0.06, and 0.09 M solutions. The synthesized products are abbreviated as Mo/SBA-15(A), Mo/SBA-15(B), and Mo/SBA-15(C) with Mo loadings of 8, 13, and 17 wt%, respectively, and were stored in dried air.

Sample characterization

Powder X-ray diffraction (XRD) patterns were obtained on a Bruker D8 Advance diffractometer at room temperature using Cu Kα radiation generated at 40 kV and 30 mA. Fourier transform (FT) Raman spectra were recorded with a Bruker FT-106 Raman module, equipped with a Ge detector cooled by liquid nitrogen, and connected to a Bruker FT-IR 66 interferometer and a continuous wave diode-pumped Nd:YAG Laser with a radiation wavelength of 1,064 nm (9398.5 cm^{-1}). The laser power was set to 300 mW and the spectral resolution was 2 cm^{-1}. Nitrogen adsorption measurements were carried out at 77 K on a Sorptomatic 1990 adsorption analyzer. Before the

measurements, the samples were outgassed for at least 24 h at 120 °C. The BET surface areas were calculated from p/p_0 = 0.03–0.3 in the adsorption branch; the BJH pore size distributions were calculated from the desorption branch.

For TEM, dried SBA-15 and MoO_3/SBA-15 powders were sonicated in dichloromethane for several seconds, dropped on the TEM grids, and dried on carbon-film-coated copper grids (Ted Pella) in air. Transmission electron microscopy microphotographs were obtained on a JEOL JEM-2000 FX electron microscope operating at 200 kV. HAADF images were obtained in a VG HB501UX dedicated scanning transmission electron microscope. In this imaging mode, the brightness is proportional to Z^n, where Z denotes the atomic number and $n \approx 1.7$. This allows distinguishing Mo from the SBA-15 support. The Mo-content was determined by EDXS with a spatial resolution of about 1 nm.

The XAS experiment was performed at the INE beamline at the ANKA 2.5 GeV synchrotron radiation facility. For details about the instrumentation at this beamline see Ref. [35]. For energy monochromatization, a Lemonnier-type [36] double-crystal monochromator equipped with Ge(422) crystals was employed, leading to a minimum energy step width of 0.2 eV. For calibration, photon energy of 20 keV was assigned to the first inflection point of the K-edge spectrum of a molybdenum foil. The absorption spectra of the powder samples: MoO_3/SBA-15 with 8 wt% molybdenum loading and MoO_3 reference were recorded at the Mo–K edge (20 keV) in transmission mode between 19.799 keV and 20.853 keV with energy steps of 0.5 eV and 2 s integration time per step.

X-ray absorption fine structure (XAFS) analysis was performed using the software WinXAS v3.1 [37]. Background subtraction and normalization were carried out by fitting linear polynomials to the pre-edge and the post-edge region of the absorption spectra, respectively. The extended X-ray absorption fine structure (EXAFS) $\chi(k)$ was extracted by using cubic splines to obtain a smooth atomic background, $m_0(k)$, where k denotes a reciprocal space vector. The pseudo-radial distribution function FT($\chi(k)*k^3$) was calculated by Fourier transforming the k^3-weighted experimental $\chi(k)$ function, multiplied by a Bessel window, into reciprocal space. EXAFS data analysis was performed using theoretical backscattering phases and amplitudes calculated with the ab-initio multiple-scattering code FEFF7 [38]. Single scattering and multiple scattering paths in the α-MoO_3 model structure were calculated up to 5.0 Å with a lower limit of 2.0% in amplitude with respect to the strongest backscattering path. EXAFS refinements were performed in reciprocal space simultaneously to magnitude and imaginary part of a Fourier-transformed k^3-weighted and k^1-weighted experimental $\chi(k)$ using the standard EXAFS formula [39]. Structural parameters that are determined by a least-squares EXAFS refinement of a MoO_3 model structure to the experimental spectra are (i) an overall shift of E_0, (ii) Debye-Waller factors for single-scattering paths, and (iii) distances of single-scattering paths. Coordination numbers (CN) and S_0^2 were kept invariant in the refinement.

Results and discussion

Powder X-ray diffraction

Figure 1 shows the X-ray powder diffraction patterns of MoO_3/SBA-15 displaying the three characteristic reflections (100), (110), and (200) of hexagonal mesoporous SBA-15 with space group *P6mm*. The powder diffraction patterns indicate that the primary structure of SBA-15 consists of well-ordered channels, which are maintained after the formation of MoO_3 nanoparticles inside the channels. In addition, the phase cancellation between the pore walls and the guest species MoO_3 leads to a decrease of the intensity of Bragg reflections, which is more pronounced for higher MoO_3 contents. This phenomenon is well known [17, 40] and was also observed in [30].

In Fig. 2, wide-angle XRD patterns of the MoO_3/SBA-15 samples along with a diffraction pattern of a physical mixture of MoO_3 and SBA-15 are displayed. Below 13 wt% Mo, no reflections of crystalline MoO_3 occur in the patterns and only a broad feature caused by SBA-15 is observed, indicating that the crystallite size of the MoO_3 particles is below the coherence length of X-ray scattering of roughly 5 nm (see Fig. 2, trace (a) with 8 wt% Mo as an example). Some weak reflections of α-MoO_3 are visible at a loading of 13 wt% Mo, and the reflection positions agree

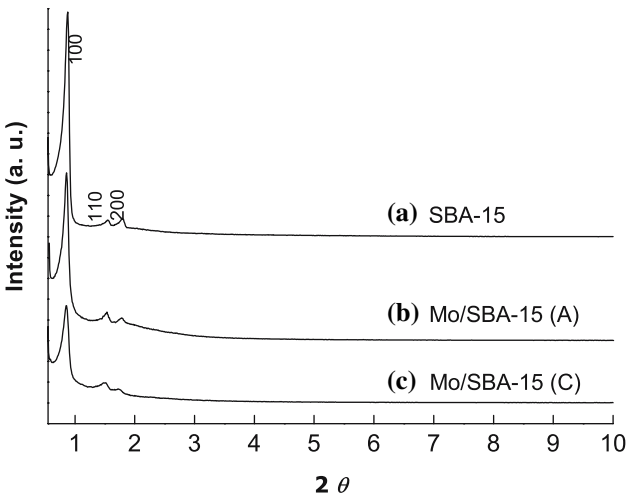

Fig. 1 XRD patterns of (**a**) SBA-15, (**b**) Mo/SBA-15(A), and (**c**) Mo/SBA-15(C) with Mo loadings of 8 wt% and 17 wt% respectively

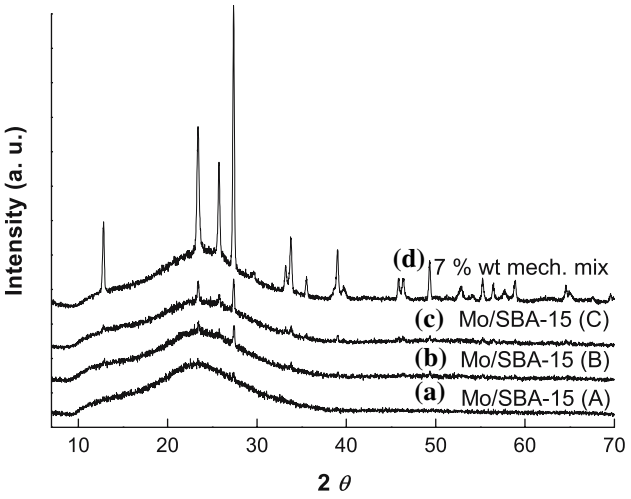

Fig. 2 XRD patterns of (**a**) Mo/SBA-15(A) (8 wt% Mo), (**b**) Mo/SBA-15(B) (13 wt% Mo), (**c**) Mo/SBA-15(C) (17 wt% Mo), and (**d**) of a physical mixture (7 wt% Mo)

well with those of bulk MoO_3. For higher loading than 13 wt% Mo, the reflections of α-MoO_3 become more intense. But even for 17 wt% Mo in the SBA-15 pores, the reflection intensity is much lower compared to the data of the mechanical mixture which has only 7 wt% Mo. The average particle size of MoO_3 can be estimated from the peak width using the Scherrer formula. The average crystallite size estimated from the reflection at $2\theta = 23.4°$ is about 30 nm for high Mo loading of 17 wt%. Comparing the size of MoO_3 with the pore diameters of the SBA-15 material suggests that the MoO_3 crystallites are located partly outside the channels of SBA-15. The amount of crystalline dispersed MoO_3 can be estimated from the intensity of the XRD reflection located at $2\theta = 23.4°$. Since the intensity of Mo/SBA-15(C) with 17 wt% Mo is nearly identical with that of a mechanical mixture of 2.5 wt% Mo (not shown), one may estimate that the amount of nanocrystalline MoO_3 for this sample is close to 14.5 wt% Mo. Indeed, the maximal loading achieved can be evaluated to 1.9 μmol m^{-2} (surface area of SBA-15 is about 850 m^2 g^{-1}) for a fully-dispersed MoO_3, which is in good agreement with the value determined by Blanchard et al. (2 μmol m^{-2}) for SBA-15 support [31]. The results of the XRD investigations clearly indicate that the MoO_3 species are finely dispersed and a similar observation was made by Dhar et al. [30].

Nitrogen physisorption

Figure 3 displays the N_2 adsorption–desorption isotherms (at 77 K), the pore-size distribution of SBA-15 and the MoO_3-impregnated SBA-15 materials with different Mo concentrations. The numerical data are listed in Table 1. For all materials, a type-IV isotherm is observed, which is the typical hysteresis loop of mesoporous materials [41], indicating that the incorporation of Mo species does not destroy the structure of mesoporous SBA-15. The pore sizes were calculated from the desorption branch of the isotherm using the Barrett-Joyner-Halenda (BJH) model, which is an appropriate method for determining changes in the pore-size distribution [17, 18, 42] and the Barrett-Emmett-Teller (BET) equation was applied for calculation of specific surface areas. The isotherms have the following characteristic features: (1) the capillary condensation step, which is caused by the decrease of the pore sizes, typically at the relative pressure $p/p_0 = 0.6–0.7$ for pristine SBA-15, shifts to lower relative pressure $p/p_0 = 0.4–0.6$ after introduction of MoO_3 particles into the pores (Fig. 3a); (2) the amount of adsorbed nitrogen decreased significantly, which is associated with the smaller specific surface area; (3) the pore volumes decrease with increasing amount of impregnated Mo in SBA-15 (Table 1) and the mean pore diameter (Fig. 3b) decreases as evidenced by the slight shift of the main peak in pore-size distribution curves to smaller values; (4) adsorption of intra-wall micropores at low relative pressures decreases with the increasing loading of MoO_3; (5) a small sub-step at the relative pressure at about 0.45 can be observed.

From the isotherms, it can be concluded that the mesoporosity of the support is still preserved after the

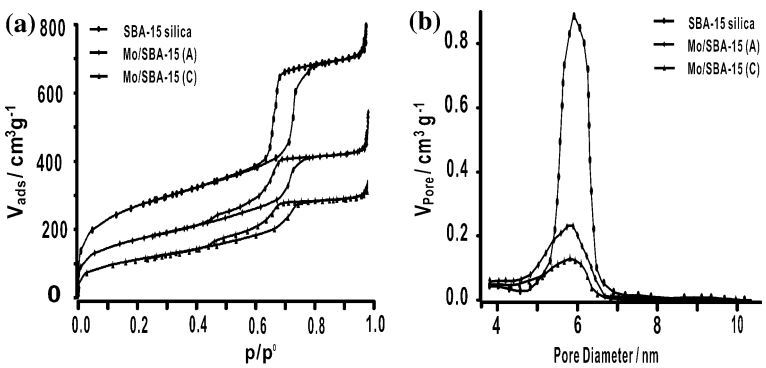

Fig. 3 Nitrogen absorption/desorption isotherms of Mo/SBA-15(A) (8 wt% Mo), Mo/SBA-15(C) (17 wt% Mo) (**a**), and BJH pore-size distribution (**b**)

Table 1 BET surface area, mean pore diameter D, and wall thickness t (calculated from $t = a–D$ [18], a = cell parameter), for the pristine SBA-15 silica and the MoO_3/SBA-15 host–guest compounds

Sample	Mo loading wt%	Mesopore/micropore volume ($cm^3\ g^{-1}$)		BET surface area ($m^2\ g^{-1}$)		Mean pore diameter D (nm)	Wall thickness t (nm)
			Normalized		Normalized		
SBA-15	0	1.08/0.17	1	920	1	5.96	4.31
Mo/SBA-15(A)	8	0.65/0.13	0.68/0.86	597	0.74	5.34	4.93
Mo/SBA-15(B)	13	0.55/0.11	0.63/0.80	505	0.68	5.11	5.16
Mo/SBA-15(C)	17	0.45/0.08	0.56/0.61	397	0.58	5.02	5.25

Normalized$(X) = X_{MoO_3}/((1-y)X_{SBA-15})$, where X is specific surface area or pore volume and y is weight fraction of MoO_3

incorporation of MoO_3 particles into the SBA-15 materials. The important decrease in pore volume (mesopores and micropores) and the reduced mean pore sizes (see Table 1) indicates the filling of both the mesopores and the micropores by MoO_3 particles. The two-step desorption branch [43] and the decrease in pore volume might be attributed to the presence of a pore-blocking effect by MoO_3, because the formation of MoO_3 particles inside the pores of SBA-15 would not significantly affect the pore volume due to the high density of MoO_3 (4,700 kg cm^{-3}). This blocking effect becomes more pronounced with increasing Mo loadings.

Transmission electron microscopy

Transmission electron microscopy was performed to analyze the microstructure of the samples. For all samples with different Mo loadings, the hexagonally ordered pore structure of the SBA-15 host was maintained after inclusion of MoO_3 and calcination. This is exemplified by the bright-field images of Fig. 4 (loading: 17 wt% Mo, two distinct magnifications), which were recorded perpendicular to the channel axes. The presence of MoO_3 inside the pores can be demonstrated by a combined approach of HAADF and EDXS. The HAADF images of Fig. 5 (17 wt% Mo) were recorded in two distinct orientations of the channels. For the image recorded perpendicular to the channel axes (Fig. 5a), randomly distributed bright spots are preferably aligned along the channel axes. In case of images along the channels axis (i.e., [001]) (Fig. 5b), bright spots fill the space of the open SBA-15 pores. Figure 6 shows EDXS spectra acquired from the bright spots (a) and from darker areas (b). It is obvious that the intensity of the Mo-L peak is significantly higher at the position of the bright spots. Occasionally, the locations of the bright spots do not fit with the periodicity of the host. The most probable interpretation here is to assume the presence of MoO_3-nanoparticles on the surface of the host. But it appears that most MoO_3-nanoparticles are located inside the SBA-15 pores.

Raman spectroscopy

Raman spectroscopy is one of the effective methods to probe crystalline and amorphous nanoscale oxides [23, 24]. Raman spectra of the impregnated samples before calcination are displayed in Fig. 7, and the characteristic bands of the $[Mo_7O_{24}]^{6-}$ anion are clearly visible for the sample with 8 wt% Mo. The strong band at 943 cm^{-1} is due to the symmetric stretching of the short Mo–O terminal bonds of $[Mo_7O_{24}]^{-6}$ along with a weak and medium band at 898 cm^{-1} [22]. The bending vibration at 362 cm^{-1} and

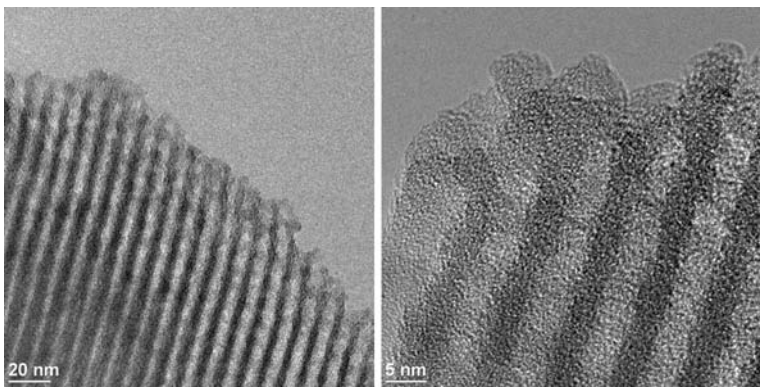

Fig. 4 TEM images with different magnifications recorded for the sample with 17 wt% Mo

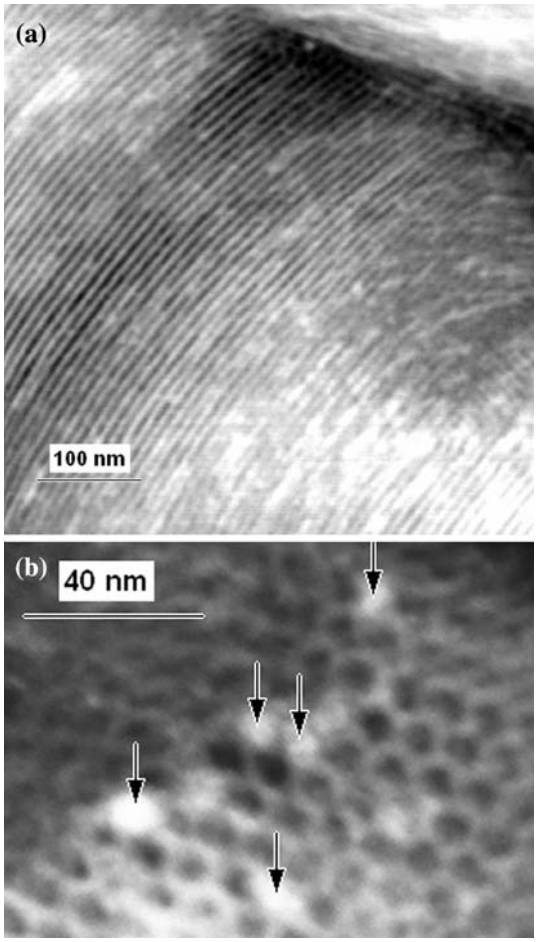

Fig. 5 HAADF images of Mo/SBA-15 (17 wt% Mo) in an orientation (**a**) perpendicular to and (**b**) along the channel axes. MoO_3-nanoparticles show bright contrast as indicated by the arrows in (b)

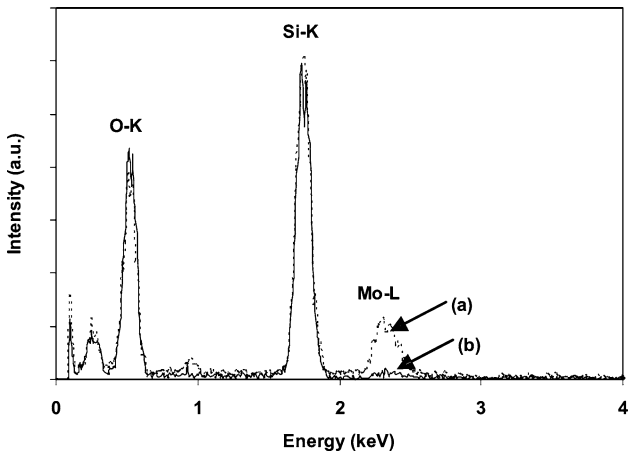

Fig. 6 Energy-dispersive X-ray spectra of (**a**) MoO_3 particle and (**b**) SBA-15

deformation band at 320 cm^{-1} of the terminal Mo=O groups are also observed. The intensity of these bands increases with the amount of incorporated AHM.

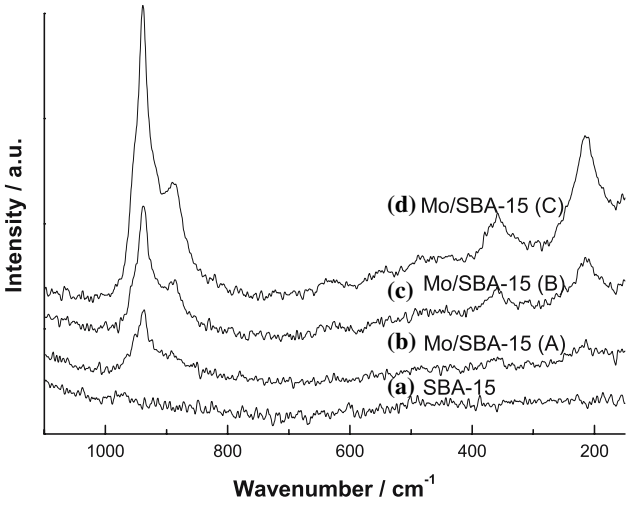

Fig. 7 Raman spectra of (**a**) SBA-15, (**b**) Mo/SBA-15(A) (8 wt% Mo), (**c**) Mo/SBA-15(B) (13 wt% Mo), and (**d**) Mo/SBA-15(C) (17 wt% Mo) before calcination at 500 °C

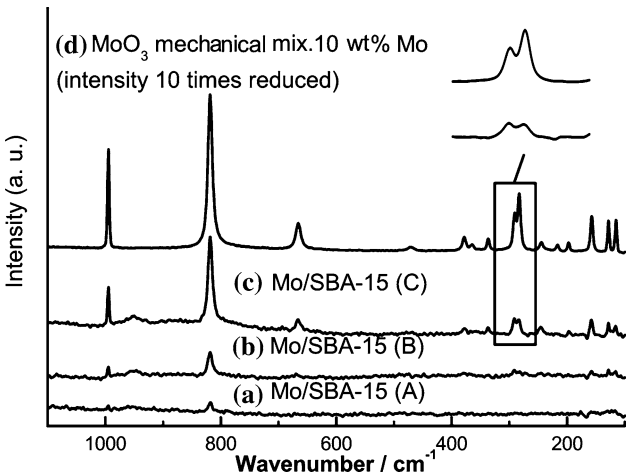

Fig. 8 Raman spectra of (**a**) Mo/SBA-15(A) (8 wt% Mo), (**b**) Mo/SBA-15(B) (13 wt% Mo), (**c**) Mo/SBA-15(C) (17 wt% Mo) after calcination, and (**d**) of a mechanical mixture (10 wt% Mo)

In the Raman spectra of calcined Mo/SBA-15 along with a spectrum of the mechanical mixture (Fig. 8), the characteristic features of bulk MoO_3 are seen. Considering only Mo–O bonds up to 2 Å, MoO_3 chains are directed along the crystallographic *c* axis by corner sharing of MoO_4 tetrahedra [44]. The Raman spectrum of MoO_3 between 82 and 995 cm^{-1} was investigated by Py and Maschke [45], who carried out a study on single crystals and performed valence force-field calculations. The band at 994 cm^{-1} was assigned to the symmetric stretching mode of the terminal Mo=O groups and the signals at 819 and 665 cm^{-1} to the vibrations of the Mo–O–Mo bridge. The doublet at 290–280 cm^{-1} corresponds to the two wagging modes of the terminal Mo=O groups.

In the spectrum of Mo/SBA-15(A) with 8 wt% Mo, only two bands are visible at 819 and 994 cm^{-1} as weak signals. For low loadings, the predominant silica-supported molybdenum species were observed to be isolated molybdate tetrahedra [21]. However, no bands at 988 and 620 cm^{-1} characteristic of MoO_4^{2-} were detected in our sample, indicating that MoO_3 should be formed as the majority species under our experimental conditions. At high loadings, the observed wave numbers for MoO_3/SBA-15 materials are similar to that found for the physical mixture. However, some features in the Raman spectra should be highlighted. The Raman spectra of MoO_3/SBA-15 materials exhibit a significant intensity loss compared to the physical mixture with the same Mo content. The intensity reduction may be explained by a reduced effective scattering volume of dispersed MoO_3 particles. Such a size-dependent intensity change was also reported by Mestl et al. [20]. Furthermore, the spectra show a change of the relative intensity of the MoO_3 characteristic modes at 819 and 994 cm^{-1}, which may be associated with the weak interaction between the highly distorted small MoO_3 particles and the SBA-15 support. The typical intensity ratio I_{994}/I_{819} for Mo/SBA-15(B) and Mo/SBA-15(C) is 0.45, which is smaller than that of the mechanical mixture of 0.64. An identical feature was observed by Braun et al. [19] and Jeziorowski et al. [46], who prepared the silica supported MoO_3 by thermal spreading (I_{994}/I_{819} = 0.49) and the impregnation method (I_{994}/I_{819} = 0.46), respectively. In addition, an interesting phenomenon in the Raman spectra is the change in relative intensity of the two wagging modes at 290 (B_{2g}) and 280 cm^{-1} (B_{3g}). In the single crystal and the physical mixture spectra, the B_{3g} wagging mode has only 2/3 of the intensity of the B_{2g} mode. For all the MoO_3/SBA-15 samples, the B_{3g} wagging mode is as intense as the B_{2g} signal and the two modes are hardly resolved. This observation is consistent with a phenomenon, which has been discussed by Braun et al. [19] in the spectra of Mo/Al_2O_3 and Mo/SiO_2 sample. The two wagging modes of the terminal Mo=O groups are parallelly polarized to the direction of the chain of the tetrahedral MoO_4 units, i.e., directed along the *c*-axis. Therefore, the change in the intensity ratio for this doublet may be attributed to the distortions along the MoO_4 chains. Finally, a weak shoulder appears at about 953 cm^{-1} corresponding to the Mo=O vibration of a polymeric molybdate species interacting with the support [24].

XAFS

The XRD patterns confirm the formation of α-MoO_3 at high Mo-loadings, and Raman data indicate the interaction of size-reduced MoO_3 with the silica support. However, the modification of MoO_3/SBA-15 at low concentration of Mo stayed unknown and was furthermore examined by XAFS. The Mo–K edge XANES spectra of MoO_3/-SBA-15(A) (8 wt% Mo), α-MoO_3, and hex-MoO_3 are depicted in Fig. 9. The similarity of the local structure around the Mo atoms in α-MoO_3 and hex-MoO_3 (Table 2) is readily visible in a very similar near-edge structure. However, in particular the feature at ~20.03 keV (arrow in Fig. 9) appears to be more reduced in the spectrum of hex-MoO_3 than in that of α-MoO_3. Compared to the references, the XANES spectrum of MoO_3/SBA-15 exhibits a similar overall shape. While the number of peaks in the XANES spectrum of MoO_3/SBA-15 is the same as in those of α-MoO_3 and hex-MoO_3, the amplitude of the peaks is significantly reduced. This holds particularly for the peak at ~20.03 keV. In total, the Mo–K edge spectra of MoO_3/SBA-15 seem to correspond to a local structure similar to that of α-MoO_3 and/or hex-MoO_3. The reduced amplitude of XANES can be attributed to a considerably reduced ordering of small particles.

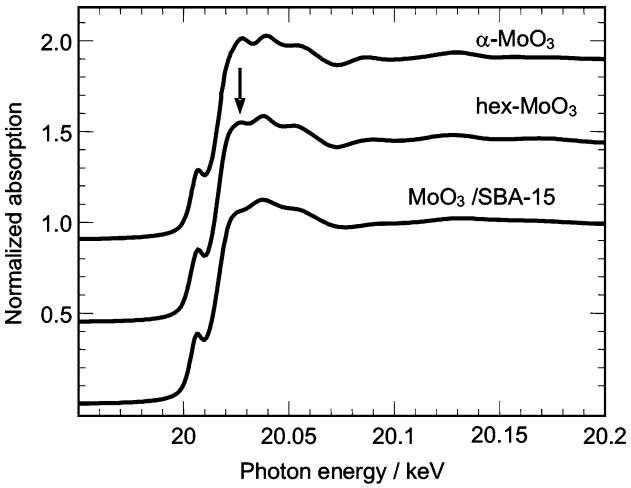

Fig. 9 Mo–K edge XANES spectra of MoO_3-SBA-15 (8 wt% Mo), α-MoO_3, and hex-MoO_3

The Fourier-transformed XAFS $\chi(k)*k^3$ of MoO_3/SBA-15(A) (8 wt% Mo), α-MoO_3, and hex-MoO_3 are shown in Fig. 10. Compared to the XANES spectrum, more distinct differences can be seen in the FT($\chi(k)*k^3$) of α-MoO_3 and hex-MoO_3. Particularly the shape of the peaks between 1.0 Å and 2.0 Å (not phase-shift corrected) that correspond to Mo–O distances and the position of the peak at ~3 Å that corresponds to Mo–Mo distances differ significantly. Compared to the references, the overall shape of the FT($\chi(k)*k^3$) of MoO_3/SBA-15 appears to resemble more closely to that of hex-MoO_3 than to that of α-MoO_3.

For a more detailed analysis of the XAFS data, the theoretical FT($\chi(k)*k^3$) calculated for an α-MoO_3 model structure was refined using the experimental spectra of

Table 2 Type and number (N) of atoms at distance R from the Mo atoms in α-MoO_3 and hex-MoO_3 model systems compared to experimental distances and EXAFS Debye-Waller factors

Type	N	Model α-MoO_3	Model hex-MoO_3	hex-MoO_3		MoO_3-SBA-15	
		R (Å)	R (Å)	R (Å)	σ^2 (Å^2)	R (Å)	σ^2 (Å^2)
Mo–O	1	1.67	1.68	1.68	0.0010	1.68	0.0010
Mo–O	1	1.73	1.73	1.75	0.0035	1.75	0.0030
Mo–O	2	1.95	1.97	1.97	0.0035	1.99	0.0065
Mo–O	1	2.25	2.20	2.21	0.0012	2.23	0.0030
Mo–O	1	2.33	2.39	2.38	0.0026	2.39	0.0021
Mo–Mo	2	3.44	3.31	3.33	0.0050	3.30	0.0080
Mo–Mo	2	3.70	3.73	3.70	0.0026	3.79	0.0083
Mo–Mo	2	3.96	4.03	3.95	0.0031	4.00	0.0101

Experimental parameters were obtained from a refinement of a α-MoO_3 model structure to the experimental Mo–K edge XAFS $\chi(k)$ of hex-MoO_3 and MoO_3/SBA-15 (8 wt% Mo) (k-range from 3.1 Å^{-1} to 14.3 Å^{-1}, R range from 0.9 Å to 4.0 Å, E_0 (MoO_3/SBA-15) = –1.5 eV, E_0 (hex-MoO_3) = –1.8 eV, residual = 6.9, N_{ind} = 24, N_{free} = 15). The uncertainty in the distances amounts to about 0.03 Å

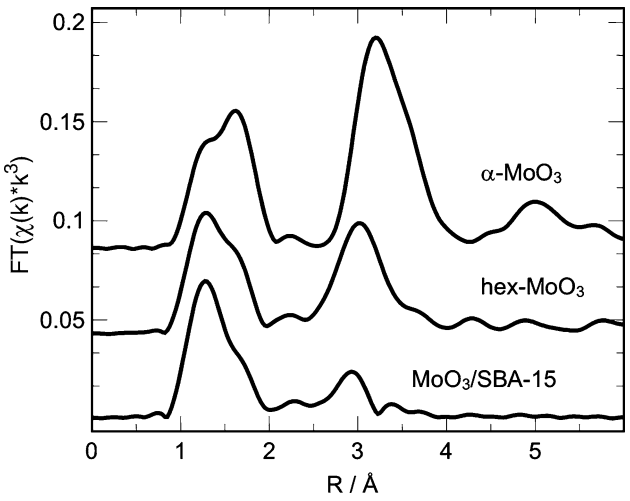

Fig. 10 Fourier transformed Mo-K edge XAFS $\chi(k)*k^3$ (not corrected for phase-shifts) of MoO_3-SBA-15 (8 wt% Mo), α-MoO_3, and hex-MoO_3

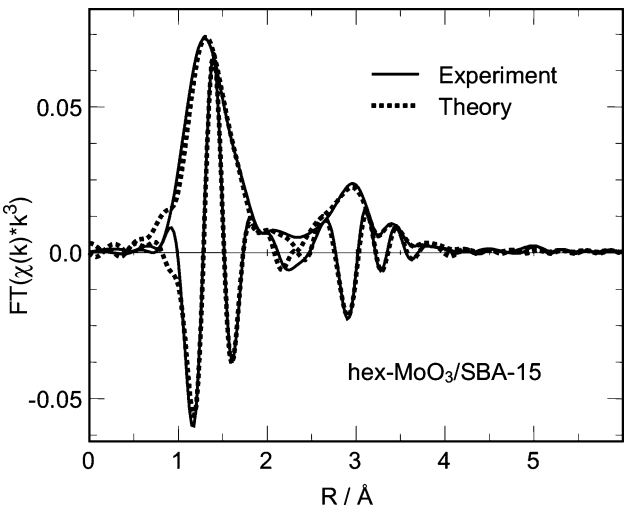

Fig. 11 Experimental and theoretical Fourier transformed Mo–K edge XAFS $\chi(k)*k^3$ (not corrected for phase-shifts) of MoO_3-SBA-15 (8 wt% Mo)

MoO_3-SBA-15 and hex-MoO_3 (Fig. 11). Therefore, the most prominent Mo–O and Mo–Mo single scattering paths were included. The refinement of the model structure to the spectrum of MoO_3/SBA-15 results in a very good agreement between the experimental and theoretical spectrum (Fig. 11). The structural parameters obtained are given in Table 2. Besides small differences in the local structure around the Mo atoms in α-MoO_3 and hex-MoO_3, a significantly shortened Mo–Mo distance of 3.3 Å exists in hex-MoO_3 compared to 3.4 Å in α-MoO_3. This short Mo–Mo distances account for the shift in peaks at higher distances as visible in the FT($\chi(k)*k^3$) of the two references. Similar to hex-MoO_3, MoO_3/SBA-15 exhibits a short Mo–Mo distance at ~3.3 Å and a slightly prolonged Mo–O distance at ~2.4 Å. The good agreement between the structural parameters of MoO_3/SBA-15 and hex-MoO_3 indeed indicates the presence of hex-MoO_3 inside the pore structure of SBA-15. The strongly reduced amplitude in the FT($\chi(k)*k^3$) at higher distances may be caused by very small particles or a predominantly two-dimensional structure of the hexagonal MoO_3 modification in SBA-15. Treating AHM in air at 500 °C results in the formation of α-MoO_3, as previously reported [33], and hex-MoO_3 is formed as an intermediate phase at ~350 °C. However, hex-MoO_3 transforms upon further heating into the more stable α-MoO_3 modification. For the materials with low Mo-loading studied here, the metastable hexagonal modification of MoO_3 appears to be

stabilized by the interaction with the SBA-15 support material.

Conclusions

AHM dissolved in water is a useful Mo precursor, which can be readily introduced into the channels of SBA-15 without destroying the structure of mesoporous SBA-15 materials (XRD, TEM, and N_2 physisorption). The formation of the $[Mo_7O_{24}]^{6-}$ anion is observed in Raman spectra prior to calcination. After conversion of AHM to MoO_3 by a heat treatment, the Raman spectra show strong effects of the reduced dimensions of MoO_3 nanosized particles onto the vibrational properties. The appearance of a weak shoulder at about 953 cm^{-1} indicates that MoO_3 particles on the pore surface of SBA-15 form $(MoO_3)_n$ oligomers. The intensity of the reflections in the XRD patterns with increasing Mo content, the reduction of the pore volumes and of the surface areas obtained from the N_2 physisorption experiments reveal that MoO_3 particles are introduced into the channels of SBA-15. This is also confirmed by the application of HAADF technique combined with EDXS. In the wide-angle XRD patterns, reflections of α-MoO_3 appear only at high loadings of more than 13 wt% Mo, i.e., for lower MoO_3 contents the particle size is far below the coherence length of X-rays. This is further evidenced by comparing the powder pattern of a physical MoO_3/SBA-15 mixture (7 wt% Mo) with that of SBA-15 materials with MoO_3 in the pores. The reflections of the mixture are much more intense than that of the material containing 17 wt% Mo. For higher Mo loading than 13 wt%, the reflections of α-MoO_3 become more intense with increasing MoO_3 content. However, at low Mo loading, the metastable hexagonal modification of MoO_3 appears to be stabilized by the interaction with the SBA-15 support material, which is clearly confirmed by the results of the EXAFS data analysis. Further experiments are under way to test the new materials in different catalytic reactions and as sensor materials.

Acknowledgements The financial support of the Deutsche Forschungsgemeinschaft (DFG), the Fonds der chemischen Industrie (FCI), and the State Schleswig-Holstein is gratefully acknowledged.

References

1. Zhao DY, Huo QS, Feng JL, Chmelka BF, Stucky GD (1998) J Am Chem Soc 120:6024
2. Zhao D, Feng J, Huo Q, Melosh N, Fredrickson GH, Chmelka BF, Stucky GD (1998) Science 279:548
3. Han YJ, Kim JM, Stucky GD (2000) Chem Mater 12:2068
4. Yang C, Liu P, Ho Y, Chiu C, Chao K (2003) Chem Mater 15:275
5. Fukuoka A, Araki H, Sakamoto Y, Sugimoto N, Tsukada H, Kumai Y, Akimoto Y, Ichikawa M (2002) Nano Lett 2:793
6. Wang D, Zhou WL, McCaughy BF, Hampsey JE, Ji X, Jiang Y-B, Xu H, Tang J, Schmehl RH, O'Connor C, Brinker CJ, Lu Y (2003) Adv Mater 15:130
7. Lee K-B, Lee S-M, Cheon J (2001) AdvMater 13:517
8. Li L, Shi J-L, Zhang L-X, Xiong L-M, Yan J-N (2004) Adv Mater 16:1079
9. Yuranov I, Kiwi-Minsker L, Buffat P, Renken A (2004) Chem Mater 16:760
10. Konya Z, Puntes VF, Kiricsi I, Zhu J, Ager JW, Ko MK, Frei H, Alivisatos P, Somorjai GA (2003) Chem Mater 15:1242
11. Yan WF, Chen B, Mahurin SM, Hagaman EW, Dai S, Overbury SH (2004) J Phys Chem B 108:2793
12. Luan ZH, Maes EM, van der Heide PAW, Zhao DY, Czernuszewicz RS, Kevan L (1999) Chem Mater 11:3680
13. Gao F, Lu QY, Liu XY, Yan YS, Zhao DY (2001) Nano Lett 1:743
14. Xu W, Liao YT, Akins DL (2002) J Phys Chem B 106:11127
15. Hsueh HS, Yang CT, Zink JI, Huang MH (2005) J Phys Chem B 109:4404
16. Yang CT, Huang MH (2005) J Phys Chem B 109:17842
17. Brieler FJ, Grundmann P, Fröba M, Chen LM, Klar PJ, Heimbrodt W, von Nidda HAK, Kurz T, Loidl A (2004) J Am Chem Soc 126:797
18. Brieler FJ, Fröba M, Chen LM, Klar PJ, Heimbrodt W, von Nidda HAK, Loidl A (2002) Chem-Eur J 8:185
19. Braun S, Appel LG, Camorim VL, Schmal M (2000) J Phys Chem B 104:6584
20. Mestl G, Srinivasan TKK, Knözinger H (1995) Langmuir 11:3795
21. Kakuta N, Tohji K, Udagawa Y (1988) J Phys Chem 92:2583
22. Desikan AN, Huang L, Oyama ST (1991) J Phys Chem 95:10050
23. Li W, Meitzner GD, Borry R III, Iglesia E (2000) J Catal 191:373
24. Stampfel SR, Chen Y, Dumesic JA, Niu C, Hill CG (1987) J Catal 105:445
25. Ono T, Anpo M, Kubokawa Y (1986) J Phys Chem 90:4780
26. Liu T-C, Forissier M, Coudurier G, Védrine JC (1989) J Chem Soc Faraday Trans 85:1607
27. Giordano N, Meazza M, Castellan A, Bart JCJ, Ragaini V (1977) J Catal 50:342
28. Ressler T, Wienold J, Jentoft RE, Girgsdies F (2003) Eur J Inorg Chem 2:301
29. Louis C, Tatibouet J-M, Che M (1988) J Catal 109:354
30. Dhar GM, Kumaran GM, Kumar M, Rawat KS, Sharma LD, Raju BD, Rao KSR (2005) Catal Today 99:309
31. Sampieri A, Pronier S, Blanchard J, Breysse M, Brunet S, Fajerwerg K, Louis C, Perot G (2005) Catal Today 107–108:537
32. Vradman L, Landau MV, Herskowitz M, Ezersky V, Talianker M, Nikitenko S, Koltypin Y, Gedanken A (2003) Stud Surf Sci Catal 146:721
33. Wienold J, Jentoft RE, Ressler T (2003) Eur J Inorg Chem 6:1058
34. Murugan R, Chang H (2001) J Chem Soc Dalton 3125
35. Grunwaldt J-D, Hannemann S, Goettlicher J, Mangold S, Denecke MA, Baiker A (2005) Phys Scr T 115:769
36. Lemonnier M, Collet O, Depautex C, Esteva J-M, Raoux D (1978) Nuclear Instrum Methods 152:109
37. Ressler T (1998) J Synchrotron Radiat 5:118
38. Rehr JJ, Booth CH, Bridges F, Zabinsky SI (1994) Phys Rev B 49:12347
39. Ressler T, Brock SL, Wong J, Suib SL (1999) J Phys Chem B 103:6407
40. Fröba M, Kohn R, Bouffaud G, Richard O, van Tendeloo G (1999) Chem Mater 11:2858
41. A. IUPAC Manual of Symbols and Terminology, Part 1, Pure Appl. Chem. 31 (1972)

42. Lastoskie C, Gubbins KE, Quirke N (1993) J Phys Chem 97:4786
43. Van Der Voort P, Ravikovitch PI, De Jong KP, Benjelloun M, Van Bavel E, Janssen AH, Neimark AV, Weckhuysen BM, Vansant EF (2002) J Phys Chem B 106:5873
44. Kihlborg L (1963) Ark Kemi 21:357
45. Py MA, Maschke K (1981) Physica B+C 105:370
46. Jeziorowski H, Knoezinger H, Grange P, Gajardo P (1980) J Phys Chem 84:1825